Assessing Climate Model Projections of Anthropogenic Warming Patterns

Henri F. Drake*[1,2], Tristan Abbott[1], and Megan Lickley[1]

[1] *Massachusetts Institute of Technology, Cambridge, MA, USA*

[2] *Woods Hole Oceanographic Institution, Woods Hole, MA, USA*

Projections of future anthropogenic climate change and their uncertainties are determined by analyzing large ensembles of numerical climate models [1]. Since the late 1980s, transient climate models have projected a pronounced global warming, with relatively high warming in the Arctic and over land and low warming over the Southern Ocean [e.g. 2]. In general, confidence in climate model projections is based on their representations of physical processes and on how well they reproduce past climates [3]. However, the relationship between a model's ability to reproduce past climate changes and project future climate changes is unknown, as observations of the future are by definition unavailable. Here, we assess climate model projections of 'future' global warming patterns published in the 1995 Intergovernmental Panel on Climate Change Second Assessment Report by quantitatively comparing them to observations acquired between 1990 and 2018 [4, 5]. Observed patterns of warming follow model projections, falling within 1.64 inter-model standard deviations of the multi-model mean over most of the globe, with the exception of the West Pacific and Southern Oceans where we observe regional cooling trends associated with the 'global warming hiatus' [6]. We find a correlation between a model's ability to reproduce spatially-resolved temperature trends over the 1920-1990 hindcast period and the 1990-2018 'nowcast' period, increasing our confidence in their projections of the future and lending support to Bayesian approaches in climate modelling [7]. Climate change mitigation has now been delayed long enough for the first projections of anthropogenic global warming to be borne out in observations, dismissing claims that models are too inaccurate to be useful and reinforcing calls for climate action [8].

There are a variety of approaches for assessing general circulation models (GCMs) based on the fidelity with which they simulate past climate (hindcast skill), but little understanding as to how these assessments relate to the fidelity of their projections of future climate (forecast skill) [See Methods for a brief review of approaches and their respective limitations]. Because of this gap in understanding, it is worth revisiting

projections from early generations of climate models for which we now have contemporary observations to probe the relationship between model hindcast skill and model forecast skill. These models provide the data required for an ideal GCM verification experiment: an observed forecast period (henceforth referred to as a 'nowcast' to distinguish it from the unobserved 1990-2100 'forecast' period) spanning a time frame long enough for long-term trends to emerge above the noise of inter-annual variability [9]. In the tropics and Arctic, the projected time of emergence is roughly 30-50 years for surface air temperature trends for a signal to noise ratio of 2 [10], suggesting that nowcast verification experiments may already be possible for model projections that begin around 1990. The earliest GCM projections of anthropogenic climate change due to both the warming tendency of greenhouse gas (GHG) emissions and the cooling tendency of sulfate aerosol emissions begin in 1990 and are described by the 1995 Intergovernmental Panel on Climate Change (IPCC) in their Second Assessment Report (SAR) [4]. (See Methods for a description of the SAR models.) Here, we revisit the SAR's decades-old climate model simulations to assess the accuracy of their 'future' projections and to develop a framework for using skill metrics to quantify the relationship between climate model hindcast skill and forecast skill.

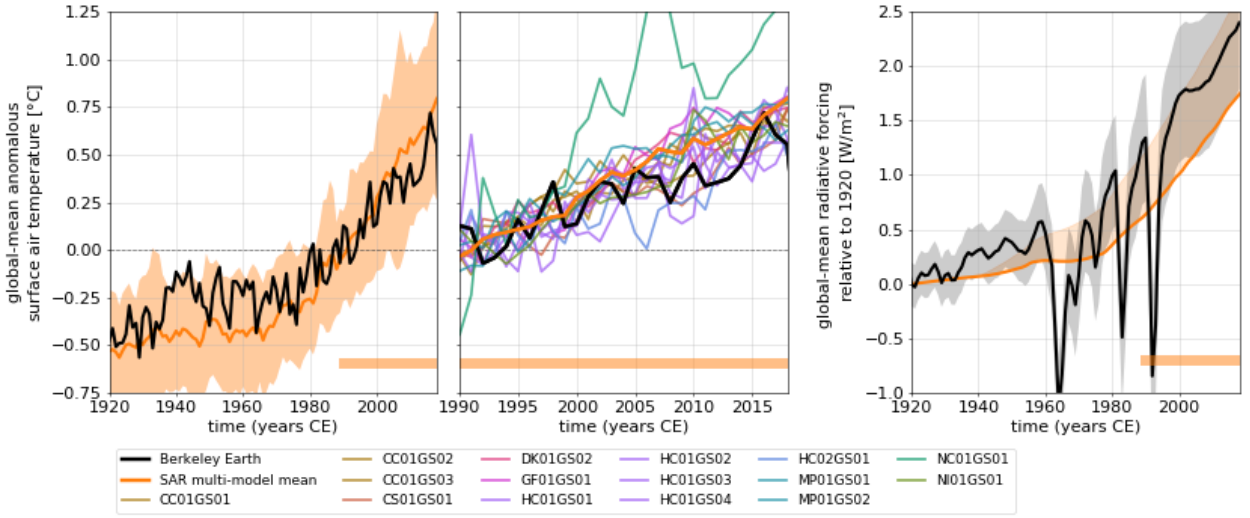

Figure 1: Projected and observed global annual mean surface air temperature anomalies and radiative forcing. (Left) Global annual mean surface air temperature anomalies relative to the 1985-1995 mean. Solid lines show the (black) Berkeley Earth observations and (orange) SAR multi-model mean. Orange shading shows the SAR multi-model mean $\pm\varsigma$, where ς is the inter-model standard deviation. (Middle) Global annual mean surface air temperature anomalies relative to the 1985-1995 mean for each individual SAR model, where colors indicate different models. (Right) Global mean radiative forcing relative to 1920. Solid lines show our estimates of historical and SAR model forcing and shading shows uncertainty estimates (see Methods for details). The orange bars delineate the 1990-2018 nowcast period.

The projected increase of radiative forcing in the SAR is of similar magnitude to modern best estimates of historical forcings, allowing us to compare the SAR models' response with the observed climate response (Figure 1, right). The SAR multi-model mean accurately reproduces the observed global-mean warming over a 1920-1990 hindcast period and accurately projects the observed global-mean warming over the 1990-2018 nowcast period (Figure 1, left). All individual models exhibit global-mean warming and inter-annual variability similar to the observations over the 1990-2018 nowcast period, except the NC01GS01 outlier model (Figure 1, middle). However, the agreement between the modelled and observed global-mean warming may be the spurious result of compensation between positive and negative biases (e.g. high climate sensitivity and low aerosol forcing [11] or high GHG forcing and high aerosol forcing [12]). Since different forcing agents have different patterns of forcing (e.g. aerosol forcing is more localized than GHG forcing), one might expect that analyzing spatial patterns of temperature trends allows for a more meaningful assessment of model skill [13]. The dependence of the temperature response pattern on the forcing patterns is muddied, however, by a relatively stronger dependence of the temperature pattern on local feedback patterns [14].

Observations during the 1990-2018 nowcast period show spatially varying temperature trends and regional emergence of warming over much but not all of the globe (Figure 2 A). We observe Arctic amplification with Arctic temperature trends of approximately 2 °C and warming that emerges throughout much of the Arctic despite large inter-annual temperature variability (Figure 2 C). Temperature increases of approximately 1 °C are common throughout both the tropics and midlatitudes, but the emergence of warming is confined largely to the tropics where inter-annual variability is small [10]. The primary exceptions to the midlatitude and tropical warming trends are: cooling in the Equatorial Pacific, the North Pacific, and Northern Eurasia (associated with natural modes of variability [6] during the 'hiatus' period or changes in patterns of aerosol loading [15]); cooling in the North Atlantic (possibly associated with forced changes in the Atlantic Meridional overturning circulation [16]); and cooling in the Southern Ocean (possibly associated with forced changes in ocean circulation [17] or underestimated natural variability [18]).

The projected SAR multi-model mean (MMM) temperature trends agree with the Berkeley Earth observations within inter-model uncertainty over the nowcast period over most of the globe, except in the West Pacific and the Southern Ocean (Figure 2 B). The MMM warming trend emerges over noise throughout the tropics largely as a result of weak inter-annual variability, as in the observations. The MMM Arctic warming trend is weaker than the observed trend and emerges above noise over less of the high-latitude northern hemisphere, but still agrees with observations to within uncertainty. The MMM projects anomalously weak warming rather than cooling in the Southern Ocean and does not project the hiatus-period West Pacific cooling signal seen in observations. Inter-model averaging is largely responsible for muted spatial variability: some but not all individual models produce widespread patterns of warming and limited regional cooling qualitatively similar to those seen in observations (Extended Data Figure 1) [as in 20]. The MMM exhibits a clear land-ocean warming contrast, as do some but not all individual models [21].

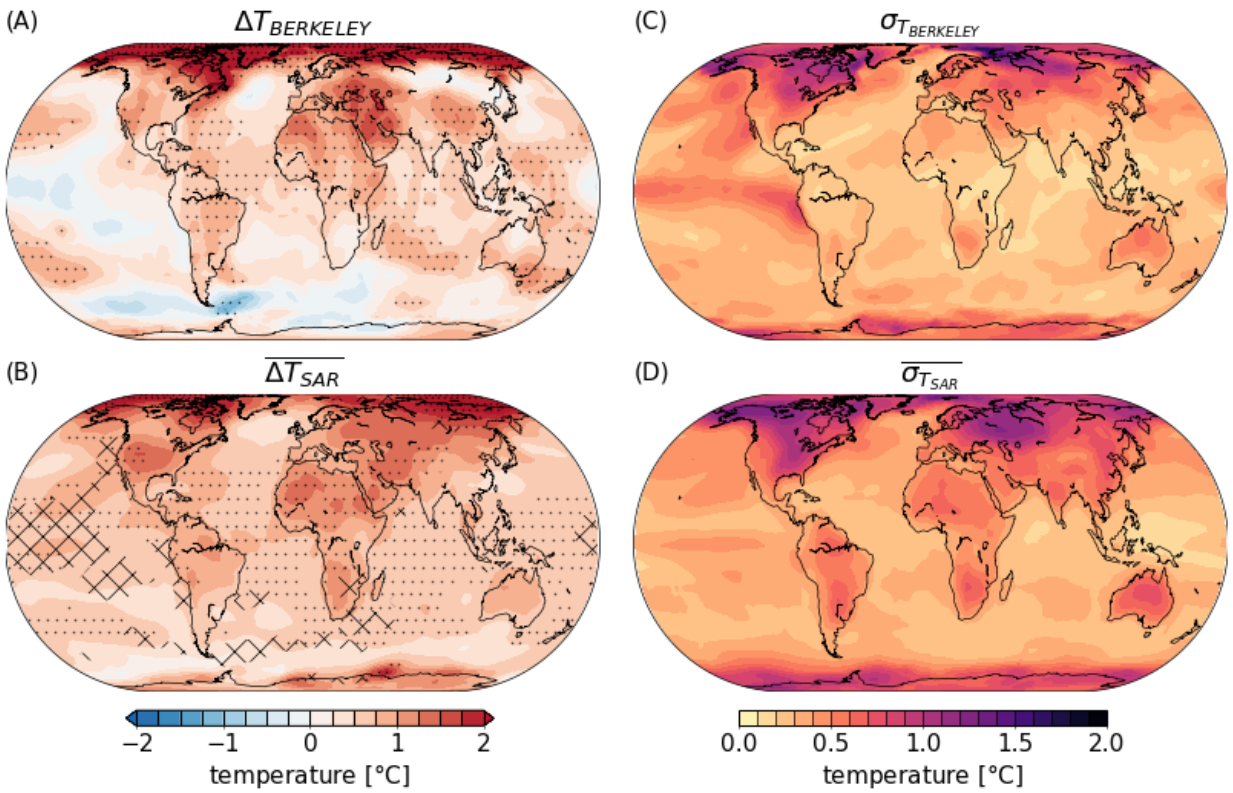

Figure 2: Observed and projected spatial patterns of temperature linear trends (expressed as a temperature change over the 28 year nowcast period) and inter-annual temperatue variability over the 1990-2018 nowcast period, linearly interpolated onto a common 3° by 3° grid. (Left) Spatial patterns of temperature trends and (Right) inter-annual variability σ, defined as the standard deviation of the annual-mean temperature timeseries with the nowcast linear trend removed, for: (A, C) the Berkeley Earth observational data set and (B, D) the SAR multi-model mean. Stippling shows where the absolute temperature trend signal has emerged above the noise of inter-annual variability, $|\Delta T| > 2\sigma$, following [10, 19]. For visual clarity, we only show stippling at every other grid cell longitude and every other grid cell latitude. Hatching shows where the observations fall outside of $\overline{\Delta T_{SAR}} \pm 1.64\varsigma$, where ς is defined as the inter-model standard deviation in linear temperature trends and $\overline{\Delta T_{SAR}}$ is the multi-model mean temperature trend.

Some individual models project temperature trends over the nowcast period more accurately than others (Extended Data Figure 1); can their nowcast skill be predicted based on their hindcast skill? To quantify the relationship between hindcast skill and nowcast skill, we compute skill metrics based on the global mean root-mean-squared model error with respect to Berkeley Earth observations for each model over the hindcast and nowcast periods [as in refs. 1, 22] (See Methods for skill metric definitions). We choose this skill metric as it reflects how well model projections capture both the magnitude and spatio-temporal patterns of observed temperature changes. We compute hindcast skill metrics based on three spatially

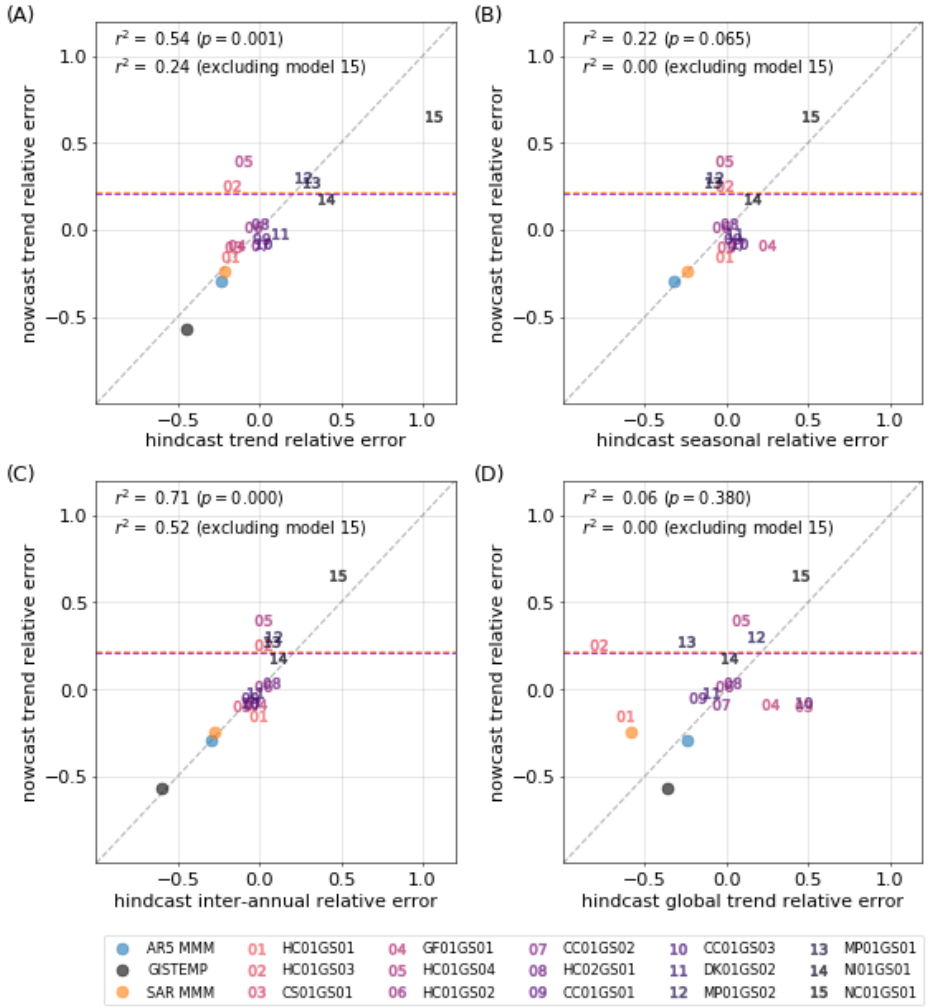

Figure 3: Correlations between skill metrics for the 1920-1990 hindcast and 1990-2018 nowcast. Y-axes show the skill metric pertaining to spatially-resolved temperature trends for the nowcast. The x-axes show four skill metrics for the hindcast: (A) a spatially-resolved temperature trend metric TREND, (B) a temperature seasonality metric SEASON, (C) an inter-annual temperature variability metric ANOM, and (D) a global-mean temperature trend metric GLOBAL (see Methods for details). Large negative values indicate high model skill, with a value of -1 indicating exact agreement with the Berkeley Earth observations. We show (blue) the AR5 multi-model mean, (black) the GISTEMP observations, (orange) the SAR multi-model mean, and (1-15) each individual SAR model. Coefficients of determination r^2 are calculated (upper) by excluding GISTEMP and the AR5 multi-model mean and (lower) additionally excluding the outlier model NC01GS01. The nearly overlapping colored dashed lines show values of the nowcast spatially-resolved temperature trend metric for two reference cases: (purple) zero trend in every grid cell and (orange) linearly extrapolating the Berkeley Earth hindcast trend patterns to the nowcast period. Note that the AR5 1990-2018 'nowcast' metric represents a combination of hindcast and nowcast since its forcing projections begin in 2005.

resolved temperature-related fields: linear trends (TREND), annual-mean anomalies of the detrended signal (ANOM), and a climatology of seasonal cycles relative to their respective annual means (SEASON). We choose these metrics to identify skill in simulating processes on decadal, annual, and monthly timescales, respectively. To highlight the information added by considering spatial patterns of trends rather than global-mean temperature trends, we also compute a hindcast skill metric based on the absolute error in global-mean temperature trends (GLOBAL). We compare all four hindcast skill metrics to the TREND metric applied to the nowcast (Figure 3). The hindcast ANOM metric, pertaining to inter-annual variability, is the metric best correlated with the nowcast TREND metric (Figure 3, C), suggesting the importance of internal modes of variability such as the Pacific Decadal Oscillation and El-Niño Southern Oscillation over the hindcast period to spatial patterns of temperature trends over the nowcast period [6]. The TREND metrics for the hindcast and nowcast periods are also correlated (Figure 3, A) and are robust to changes in the length of the hindcast interval (Figure 5, left), supporting the intuitive assumption that models which reproduce historical temperature trends are more likely to accurately project future temperature trends. The GLOBAL and SEASON metrics for the hindcast are poorly correlated with the TREND metric for the nowcast (Figure 3, B and D). The strong correlation between hindcast skill and forecast skill for the outlier model suggests that errors in multi-model mean projections could be reduced by ignoring outlier models that perform poorly on hindcast. Even with the outlier model included, though, the MMM outperforms any individual model over both the hindcast and forecast periods for all but the GLOBAL metric, supporting the common practice of using the MMM as a 'best guess' projection [1]. On the relatively short timescale of the nowcast period, however, the MMM's exceptional skill may be attributable to the attenuation of internal variability by ensemble-averaging, while individual models are instead penalized for exhibiting modes of variability out of phase with observed variability [20]. The positive correlations we find between model skill over the hindcast and nowcast periods support the community's push towards Bayesian methods of analysing climate model ensembles [7].

To benchmark the absolute skill of SAR models, we compare them to two heuristic projections of warming patterns for the nowcast: 1) uniformly-zero temperature trends and 2) a linear extrapolation of observed hindcast temperature trends at each grid cell (see Extended Data Figure 2, A). The MMM and most individual model projections are more skillful than both heuristic models (Figure 3, colored lines), independent of the length of the hindcast period used for extrapolation (Extended Data Figure 5, right). We also include a second observational product (the GISTEMP temperature dataset) as a reference point to illustrate the degree of uncertainty in our observational dataset and to indicate the potential for model improvement. Hindcast skill is slightly improved in the IPCC Fifth Assessment Report (AR5) MMM relative to the SAR MMM (Figure 3), suggesting incremental improvements in modelling hindcast temperature trends [23][see Methods for a description of the AR5 models]. We note that the incremental improvements between the SAR and AR5 may be due to an upper limit on hindcast skill set by the stochastic phasing of internal variability.

Our results build confidence in the ability of numerical climate models to project patterns of anthropogenic global warming on multi-decadal timescales. With every climate model generation come improvements in both the resolution and parameterization of climate-relevant processes [1]. Whether increasingly comprehensive climate models produce more accurate projections, however, is yet to be determined [3]. To facilitate this future work, we encourage modelling centers to archive model source code and documentation so that simulations can be re-run in their original configurations (i.e. parameter values and initial conditions) but with realized forcing scenarios prescribed retrospectively. Such retrospective simulations would allow errors in the projected climate response to be deconvoluted from errors in the projected radiative forcing, providing a more robust framework for the verification and inter-generational comparison of climate model projections. The respective contributions of internal variability and the forced response to the skill of multi-decadal model predictions could be disentangled by using 'dynamical adjustment' techniques which remove temperature anomalies induced by circulation anomalies and therefore approximate the observed and modelled forced response [24]. We expect further insights into climate model forecast skill to be gained as the first generation of coordinated decadal predictions, simulations which are initialized with observed phases of internal variability, reach maturity [25].

Methods

Approaches to climate model assessment

A straightforward approach to assessing climate models is to compare spatial patterns of simulated and observed fields over the hindcast period [eg. 26, 27]. For large model ensembles or a large number of climate variables, a common approach involves computing scalar metrics that assess model hindcast skill and can be compared across models in an ensemble, across different climate variables, and across model generations [3, 22, 28]. The implicit assumption in both approaches is that a GCM's skill at reproducing the observed past climate provides an indication of its overall physical representation of the climate system and thus its ability to forecast future climate. This, however, raises the question of whether tuning GCM parameters to reproduce the hindcast period introduces compensating model errors [29–31]. In the limit of excessive tuning, high hindcast skill may become uncorrelated (or even negatively correlated) with forecast skill. Since successive model generations perform better at such skill metrics, it is argued that "an increasing level of confidence can be placed in model-based predictions of climate", with the caveat that this is "only true to the extent that the performance of a model in simulating present mean climate is related to the ability to make reliable forecasts of long-term trends" [3]. One of our novel contributions is to quantify this relationship for temperature trends on multi-decadal timescales.

Models have also been evaluated based on their ability to reproduce paleoclimates given estimated boundary

conditions [32, 33]. Estimates of paleoclimate are considered 'out-of-sample' verification data because models are generally developed and tuned in the context of the historical hindcast period. However, this approach is limited by both uncertainties in past climate states and the viability of past climate states as analogues of transient anthropogenic climate change [33, 34].

Some models have demonstrated skill in forecasting the short term climate response to a pulse of radiative forcing, such as the volcanic eruption of Pinatubo in 1991 [eg. 35, 36]. However, it is unclear how skill in such exercises relate to skill at forecasting a multi-decadal response to sustained anthropogenic forcing. The earliest multi-decadal to centennial GCM forecasts are now being verified with respect to ensuing observations, but comparisons documented in the literature to date are either qualitative [37] or limited to global-mean variables [38, 39].

IPCC Second Assessment Report (SAR) Models

The following are the subset of coupled atmosphere-ocean general circulation models in the IPCC Second Assessment Report (SAR)[4] which have output archived in the IPCC data distribution center (`http://www.ipcc-data.org/sim/gcm_monthly/IS92A_SAR/index.html`): ECHAM3/OPYC3 (DK01) from the German Climate Computing Center [40–42]; ECHAM4/OPYC3 (MP01) from Germany's Max Plank Institute for Meteology [40–42]; HADCM2 (HC01) and HADCM3 (HC02) from the UK's Hadley Center for Climate Prediction and Research [43, 44]; CSIRO-Mk2 (CS01) from Australia's Commonwealth Scientific and Industrial Research Organization [45]; NCAR-CESM (NC01) from the USA's National Center for Atmospheric Research [46]; GFDL-R15 (GF01) from the USA's Geophysical Fluid Dynamics Laboratory [21, 47]; CGCM1 (CC01) from Canada's Center for Climate Modelling and Analysis [48, 49]; CCSR/NIES AOGCM (NI01) from Japan's Center for Climate System Research and National Insitute for Environmental Studies [50, 51]. All of the SAR models contain coupled and dynamic ocean, atmosphere, and sea-ice models. All models are flux-adjusted to avoid drift in the model mean state, except for NC01 which does not use any flux adjustments. All models are linearly interpolated to a 3° latitude by 3° longitude grid. These model runs predate the Coupled Model Intercomparison Project (CMIP), although many models are similar to versions used in CMIP1 (preindustrial control runs with constant radiative forcings) and CMIP2 (forced by 1%/year compound increase in CO_2 concentrations).

We consider SAR simulations which are forced by changes in both greenhouse gas (GHG) and sulfate aerosol concentrations. Aerosol forcings are parameterized as an increased surface albedo and represent only the aerosol direct effect. Most models approximate the radiative forcing of all GHGs with an equivalent CO_2 concentration, though some perform radiative transfer calculations for each individual gas. Before 1990, the SAR models are forced by historical GHG and anthropogenic sulfate aerosol concentrations. After 1990, GHG and aerosol concentrations evolve according to the IS92a scenario [52]. The IS92a represents a scenario

in which population rises to 11.3 billion by 2100, economic growth averages 2.3% per year, and energy is produced by a mix of fossil fuel and renewable sources, resulting in a total anthropogenic forcing of about $6\,\mathrm{W/m^2}$ above preindustrial levels by 2100. Changes in forcing due to volcanic eruptions, solar variability, and orbital oscillations are excluded in both the 1920-1990 hindcast and the 1990-2100 forecast periods. We choose to start our nowcast period in 1990 (when forcings switch from historical to projected) rather than 1996 (the SAR publication year), but our results are qualitatively similar if we instead choose to consider a 1996-2018 nowcast period. Since radiative forcing data was not archived for the SAR models, we estimate their forcing by digitizing offline calculations IS92a scenario radiative forcing from figure 6.18 of the SAR (Figure 1, solid orange line in right panel). Since these offline calculations include the indirect effect of aerosols on clouds that is not included in the SAR models, we estimate a correction to the SAR forcing by subtracting the timeseries of indirect effect forcing in Figure 6.19 of the SAR. Our estimated SAR model forcing is thus revised upwards by an amount that increases linearly from zero in 1940 to $1.15\,\mathrm{W/m^2}$ in 2040 and held constant afterwards (orange shading in right panels of figure 1 and Extended Data Figure 6). The SAR runs we use are more useful than the CMIP1/2 simulations for comparing to observations because the projected forcings over the 1990-2018 nowcast period are more similar to our best guess of realized forcings over that period (see Historical Forcings section), due to the inclusion of both the effect of increasing GHG concentrations and the direct effect of anthropogenic sulfate aerosol emissions (Figure 1, right) [13].

We calculate democratic multi-model means by assigning an equal weight to each model version so as not to weight models with several submitted runs (initial condition perturbation ensembles) more than other models. Weights are also applied to all calculations of inter-model standard deviations ς. Although we assign equal weights to each unique model, these models should not be considered fully independent samples as many share similar codes, parameterizations, and tuning data sets [28]. The interdependence of models is evident in the grouping of global-mean surface air temperature projections into two distinct branches corresponding to (upper) the North American models and (lower) all other models (Extended Data Figure 6).

IPCC Fifth Assessment Report (AR5) Models

We compare GCMs from the SAR to a subset of models from the most recent generation of CMIP models (CMIP5) from the IPPC's Fifth Assessment Report (AR5) run under the RCP 4.5 emissions scenario [53]. The AR5 model ensemble includes: Five CanESM2 ensemble members from the Canadian Centre for Climate Modelling and Analysis; Six CCSM4 ensemble members from the National Center for Atmospheric Research; Ten CSIRO-Mk3.6.0 ensemble members from the Commonwealth Scientific and Industrial Research Organization in collaboration with Queensland Climate Change Centre of Excellence; Five GISS-E2-H and six GISS-E2-R ensemble members from the NASA Goddard Institute for Space Studies; One ensemble member

each from ACCESS1.0 and ACCESS1.3 from the Commonwealth Scientific and Industrial Research Organization and Bureau of Meteorology, Australia; One ensemble member from BCC-CSM1.1 from the Beijing Climate Center, China Meteorological Administration; Four EC-EARTH ensemble members from the EC-EARTH consortium; Two FIO-ESM ensemble members from the First Institute of Oceanography, SOA, China; One ensemble member each from GFDL-CM3, GFDL-ESM2G and GFDL-ESM2M from NOAA's Geophysical Fluid Dynamics Laboratory; One ensemble member each from HadGEM2-AO and HadGEM2-CC from the Met Office Hadley Centre; Three MIROC5 ensemble members and one ensemble member each from MIROC-ESM-CHEM and MIROC-ESM from the Atmosphere and Ocean Research Institute, National Institute for Environmental Studies, and Japan Agency for Marine-Earth Science and Technology; One ensemble member from MPI-ESM-LR from the Max-Planck-Institute for Meteorology; and one ensemble member each from NorESM1-M and NorESM1-ME from the Norwegian Cliamte Centre. All models are linearly interpolated to a 3° latitude by 3° longitude grid. The democratic multi-model mean is calculated by assigning an equal weight to each model version, as described for SAR models above.

The AR5 multi-model mean (MMM) timeseries of global-mean temperature is shown in Extended Data Figure 6 (left) and the forcing timeseries associated with the RCP 4.5 scenario is shown in Extended Data Figure 6 (right). We linearly interpolate the forcing between decadal averages to get an annually-resolved timeseries. Extended Data Figure 7 puts the SAR temperature trend forecast in the context of the more modern AR5 model forecast. Because the model ensembles are forced differently over the forecast period (Extended Data Figure 6, right) and thus exhibit different magnitudes of warming (assuming similar climate sensitivities), we normalize each model's spatially-resolved linear temperature trends by its global-mean trend (Extended Data Figure 6, left). Extended Data Figure 7 C shows the normalized spatial patterns of the AR5 MMM temperature trend and Extended Data Figure 7 D shows the ensemble standard deviation ς. The spatial patterns of MMM warming in the SAR and AR5 are similar, exhibiting comparable degrees of Arctic amplification and enhanced warming over land relative to over ocean (Extended Data Figure 7 A and C for SAR and AR5 MMMs, respectively; Extended Data Figure 3 for individual SAR models). A notable difference is the lack of warming in the North Atlantic in AR5 (possibly related to differences in the slowdown of the AMOC [16]). Inter-model variance in the spatial patterns of warming is smaller in AR5 than SAR over much of the globe (Extended Data Figure 7 B, D).

Observational Products

We use the Berkeley Earth global product of surface air temperatures as observational 'truth' when assessing climate models [5], because it is most independent of data products that may have been used for tuning the SAR models. To quantify the uncertainty in the error metrics due to uncertainty in the observed temperatures, we also show the error between the Berkeley Earth observations and the GISTEMP observations [54, 55] relative to the SAR median model error (Figure 3).

Both the Berkeley Earth and GISTEMP observational products use sea surface temperatures as a proxy for surface air temperature (SAT) over the ocean, where direct SAT measurements are sparse. This causes both observational products to underestimate global-mean SAT trends by about 10% relative to estimates derived solely from SAT, such as those presented here for SAR and AR5 models [56]. We mask trends in grid cells missing more than 50% of monthly temperature values over the time period considered (e.g. over Antarctica in Extended Data Figure 2 B).

Historical Forcings

We estimate historical forcings and their uncertainties from a 200-member ensemble of adjusted forcings [57] diagnosed from historical CMIP5 simulations [53], updated for 2017 and linearly extrapolated out to 2018 (Figure 1, right). These adjusted forcings represent our best guess of the radiative forcings over the 1920-1990 historical period for which we have nearly global coverage of direct temperature observations. The adjusted forcings include the combined effects of greenhouse gases, tropospheric aerosols, stratospheric aerosols (anthropogenic and volcanic), and variations in solar forcing. Uncertainty in historical forcings is estimated by the inter-model standard deviation ς (grey shading in Figure 1, right).

Spatially-resolved skill metrics

Following [22], we measure a model m's skill based on the globally-averaged root mean square (RMS) error (E_m) between a simulated field (F_m) and the observed field (R) from Berkeley Earth. We calculate three separate RMS errors in order to distinguish between model skill at simulating: linear trends, annual-mean anomalies of the detrended signal, and a climatology of seasonal cycles relative to their respective annual means. Relative errors (I_m) for a model are calculated as

$$I_m = \frac{E_m - \overline{E}}{\overline{E}}, \tag{1}$$

where $\overline{E}$ is the SAR multi-model median error. A model field is identical to the Berkeley Earth observations if $I_m = -1$, agrees with Berkeley Earth better than the median SAR model if $-1 < I_m < 0$, and agrees with Berkeley Earth worse than the median SAR model if $I_m > 0$. All relative errors I_m are shown in Extended Data Figure 4, with a subset shown in Figure 3.

Trend RMS error

R_{ij} and F_{mij} are the linear trends in surface air temperatures (SATs) for latitude j, longitude i, and model m, calculated by linear regression of temperature against time over either the hindcast or nowcast period.

We define

$$E_m^{(t)} = \sqrt{\frac{1}{W^{(t)}} \sum_i \sum_j w_{ij}^{(t)} \left(F_{mij}^{(t)} - R_{ij}^{(t)}\right)^2}, \tag{2}$$

where $w_{ij}^{(t)}$ are grid cell-area weights and $W^{(t)} = \sum_i \sum_j w_{ij}^{(t)}$ is the global surface area.

Inter-annual RMS error

R_{ijt} and F_{mijt} are the annual-mean SATs for year t, latitude j, longitude i, and model m, with the linear trend removed at each grid cell $[i, j]$ to isolate inter-annual variability from the linear trend. We define

$$E_m^{(a)} = \sqrt{\frac{1}{W^{(a)}} \sum_i \sum_j \sum_t w_{ijt}^{(a)} \left(F_{mijt}^{(a)} - R_{ijt}^{(a)}\right)^2}, \tag{3}$$

where $w_{ijt}^{(a)}$ are the grid cell-area weights and $W^{(a)} = \sum_i \sum_j \sum_t w_{ijt}^{(a)}$ is the global surface area times the number of years t.

Seasonal Cycle RMS error

R_{ijk} and F_{mijk} are the climatological SATs for month k, latitude j, longitude i, and model m. We remove the annual-mean temperature before computing the climatology in order to remove the combined effects of interannual variability and a linear trend. We define

$$E_m^{(s)} = \sqrt{\frac{1}{W^{(s)}} \sum_i \sum_j \sum_k w_{ijk}^{(s)} \left(F_{mijk}^{(s)} - R_{ijk}^{(s)}\right)^2}, \tag{4}$$

where $w_{ij}^{(s)}$ is the product of the grid cell-area at grid cell $[i, j]$ and the length of the month k, and $W^{(s)} = \sum_i \sum_j \sum_k w_{ijk}^{(s)}$ is the global surface area times the length of the year.

Global-mean skill metric

We define the global-mean trend metric (E_m) for a model m as the absolute difference between a simulated global-mean trend (F_m) and the observed global-mean trend (R) from Berkeley Earth,

$$E_m^{(g)} = |F_m - R|. \tag{5}$$

We define the relative global-mean trend error $I_m^{(g)}$ for a model m as

$$I_m^{(g)} = \frac{E_m^{(g)} - \overline{E^{(g)}}}{\overline{E^{(g)}}}, \tag{6}$$

where $\overline{E^{(g)}}$ is the SAR multi-model median error.

Data Availability

All data files for observational and model temperature fields and post-processing source code will be publicly available at `https://github.com/hdrake/climate-model-performance` upon successful publication (or shared privately beforehand upon request by reviewer).

References

[1] Stocker, T. *Climate change 2013: the physical science basis: Working Group I contribution to the Fifth assessment report of the Intergovernmental Panel on Climate Change* (Cambridge University Press, 2014).

[2] Stouffer, R. J., Manabe, S. & Bryan, K. Interhemispheric asymmetry in climate response to a gradual increase of atmospheric CO 2. *Nature* **342**, 660 (1989). URL `https://www.nature.com/articles/342660a0`.

[3] Reichler, T. & Kim, J. How Well Do Coupled Models Simulate Today's Climate? *Bulletin of the American Meteorological Society* **89**, 303–312 (2008). URL `https://journals.ametsoc.org/doi/10.1175/BAMS-89-3-303`.

[4] Houghton, J. T. *et al. Climate change 1995: The science of climate change: contribution of working group I to the second assessment report of the Intergovernmental Panel on Climate Change*, vol. 2 (Cambridge University Press, 1996).

[5] Rohde, R. *et al.* Berkeley Earth Temperature Averaging Process. *Geoinformatics & Geostatistics: An Overview* **2013** (2016). URL `https://www.scitechnol.com/berkeley-earth-temperature-averaging-process-IpUG.php?article_id=582`.

[6] Medhaug, I., Stolpe, M. B., Fischer, E. M. & Knutti, R. Reconciling controversies about the 'global warming hiatus'. *Nature* **545** (2017).

[7] Eyring, V. *et al.* Taking climate model evaluation to the next level. *Nature Climate Change* **9**, 102 (2019). URL `https://www.nature.com/articles/s41558-018-0355-y`.

[8] Summary for policymakers. In Masson-Delmotte, V. *et al.* (eds.) *Global Warming of 1.5C. An IPCC Special Report on the impacts of global warming of 1.5C above pre-industrial levels and related global greenhouse gas emission pathways, in the context of strengthening the global response to the threat of climate change, sustainable development, and efforts to eradicate poverty* (World Meteorological Organization, Geneva, Switzerland, 2018).

[9] Hansen, J. *et al.* Global climate changes as forecast by Goddard Institute for Space Studies three-dimensional model. *Journal of Geophysical Research: Atmospheres* **93**, 9341–9364 (1988). URL https://agupubs.onlinelibrary.wiley.com/doi/abs/10.1029/JD093iD08p09341.

[10] Hawkins, E. & Sutton, R. Time of emergence of climate signals. *Geophysical Research Letters* **39** (2012). URL https://agupubs.onlinelibrary.wiley.com/doi/abs/10.1029/2011GL050087.

[11] Kiehl, J. T. & Shields, C. A. Climate simulation of the latest permian: Implications for mass extinction. *Geology* **33**, 757–760 (2005).

[12] Allen, M. R., Stott, P. A., Mitchell, J. F. B., Schnur, R. & Delworth, T. L. Quantifying the uncertainty in forecasts of anthropogenic climate change. *Nature* **407**, 617 (2000). URL https://www.nature.com/articles/35036559.

[13] Mitchell, J. F. B., Johns, T. C., Gregory, J. M. & Tett, S. F. B. Climate response to increasing levels of greenhouse gases and sulphate aerosols. *Nature* **376**, 501 (1995). URL https://www.nature.com/articles/376501a0.

[14] Boer, G. & Yu, B. Climate sensitivity and response. *Climate Dynamics* **20**, 415–429 (2003). URL https://doi.org/10.1007/s00382-002-0283-3.

[15] Smith, D. M. *et al.* Role of volcanic and anthropogenic aerosols in the recent global surface warming slowdown. *Nature Climate Change* **6**, 936–940 (2016). URL https://www.nature.com/articles/nclimate3058.

[16] Caesar, L., Rahmstorf, S., Robinson, A., Feulner, G. & Saba, V. Observed fingerprint of a weakening Atlantic Ocean overturning circulation. *Nature* **556**, 191 (2018). URL https://www.nature.com/articles/s41586-018-0006-5.

[17] Marshall, J. *et al.* The ocean's role in the transient response of climate to abrupt greenhouse gas forcing. *Climate Dynamics* **44**, 2287–2299 (2015).

[18] Jones, J. M. *et al.* Assessing recent trends in high-latitude Southern Hemisphere surface climate. *Nature Climate Change* **6**, 917–926 (2016). URL https://www.nature.com/articles/nclimate3103.

[19] Collins, M. *et al.* Chapter 12 - Long-term climate change: Projections, commitments and irreversibility. In IPCC (ed.) *Climate Change 2013: The Physical Science Basis. IPCC Working Group I Contribution to AR5* (Cambridge University Press, Cambridge, 2013). URL http://www.climatechange2013.org/images/report/WG1AR5_Chapter12_FINAL.pdf.

[20] Pierce, D. W., Barnett, T. P., Santer, B. D. & Gleckler, P. J. Selecting global climate models for regional climate change studies. *Proceedings of the National Academy of Sciences* **106**, 8441–8446 (2009). URL https://www.pnas.org/content/106/21/8441.

[21] Manabe, S., Stouffer, R. J., Spelman, M. J. & Bryan, K. Transient Responses of a Coupled Ocean–Atmosphere Model to Gradual Changes of Atmospheric CO2. Part I. Annual Mean Response. *Journal of Climate* **4**, 785–818 (1991). URL https://journals.ametsoc.org/doi/10.1175/1520-0442%281991%29004%3C0785%3ATROACO%3E2.0.CO%3B2.

[22] Gleckler, P. J., Taylor, K. E. & Doutriaux, C. Performance metrics for climate models. *Journal of Geophysical Research: Atmospheres* **113** (2008).

[23] Rauser, F., Gleckler, P. & Marotzke, J. Rethinking the Default Construction of Multimodel Climate Ensembles. *Bulletin of the American Meteorological Society* **96**, 911–919 (2014). URL https://journals.ametsoc.org/doi/10.1175/BAMS-D-13-00181.1.

[24] Deser, C., Phillips, A. S., Alexander, M. A. & Smoliak, B. V. Projecting North American Climate over the Next 50 Years: Uncertainty due to Internal Variability. *Journal of Climate* **27**, 2271–2296 (2013). URL https://journals.ametsoc.org/doi/full/10.1175/JCLI-D-13-00451.1.

[25] Meehl, G. A. *et al.* Decadal Climate Prediction: An Update from the Trenches. *Bulletin of the American Meteorological Society* **95**, 243–267 (2013). URL https://journals.ametsoc.org/doi/full/10.1175/BAMS-D-12-00241.1.

[26] Knutson, T. R., Delworth, T. L., Dixon, K. W. & Stouffer, R. J. Model assessment of regional surface temperature trends (1949–1997). *Journal of Geophysical Research: Atmospheres* **104**, 30981–30996 (1999). URL https://agupubs.onlinelibrary.wiley.com/doi/abs/10.1029/1999JD900965.

[27] Knutson, T. R., Zeng, F. & Wittenberg, A. T. Multimodel Assessment of Regional Surface Temperature Trends: CMIP3 and CMIP5 Twentieth-Century Simulations. *Journal of Climate* **26**, 8709–8743 (2013). URL https://journals.ametsoc.org/doi/10.1175/JCLI-D-12-00567.1.

[28] Knutti, R., Masson, D. & Gettelman, A. Climate model genealogy: Generation CMIP5 and how we got there. *Geophysical Research Letters* **40**, 1194–1199 (2013). URL https://agupubs.onlinelibrary.wiley.com/doi/abs/10.1002/grl.50256.

[29] Schwartz, S. E., Charlson, R. J. & Rodhe, H. Quantifying climate change — too rosy a picture? *Nature Climate Change* 23–24 (2007). URL https://www.nature.com/articles/climate.2007.22.

[30] Hourdin, F. *et al.* The Art and Science of Climate Model Tuning. *Bulletin of the American Meteorological Society* **98**, 589–602 (2016). URL https://journals.ametsoc.org/doi/full/10.1175/BAMS-D-15-00135.1.

[31] Schmidt, G. A. *et al.* Practice and philosophy of climate model tuning across six US modeling centers. *Geoscientific Model Development* **10**, 3207–3223 (2017). URL https://www.geosci-model-dev.net/10/3207/2017/gmd-10-3207-2017.html.

[32] Braconnot, P. *et al.* Evaluation of climate models using palaeoclimatic data. *Nature Climate Change* **2**, 417–424 (2012). URL https://www.nature.com/articles/nclimate1456.

[33] Harrison, S. P. *et al.* Evaluation of cmip5 palaeo-simulations to improve climate projections. *Nature Climate Change* **5**, 735 (2015).

[34] Burke, K. D. *et al.* Pliocene and Eocene provide best analogs for near-future climates. *Proceedings of the National Academy of Sciences* **115**, 13288–13293 (2018). URL https://www.pnas.org/content/115/52/13288.

[35] Hansen, J., Lacis, A., Ruedy, R. & Sato, M. Potential climate impact of Mount Pinatubo eruption. *Geophysical Research Letters* **19**, 215–218 (1992). URL https://agupubs.onlinelibrary.wiley.com/doi/abs/10.1029/91GL02788.

[36] Parker, D. E., Wilson, H., Jones, P. D., Christy, J. R. & Folland, C. K. The Impact of Mount Pinatubo on World-Wide Temperatures. *International Journal of Climatology* **16**, 487–497 (1996). URL https://rmets.onlinelibrary.wiley.com/doi/abs/10.1002/%28SICI%291097-0088%28199605%2916%3A5%3C487%3A%3AAID-JOC39%3E3.0.CO%3B2-J.

[37] Stouffer, R. J. & Manabe, S. Assessing temperature pattern projections made in 1989. *Nature Climate Change* **7**, 163–165 (2017). URL https://www.nature.com/articles/nclimate3224.

[38] Frame, D. J. & Stone, D. A. Assessment of the first consensus prediction on climate change. *Nature Climate Change* **3**, 357–359 (2013). URL https://www.nature.com/articles/nclimate1763.

[39] Rahmstorf, S., Foster, G. & Cazenave, A. Comparing climate projections to observations up to 2011. *Environmental Research Letters* **7**, 044035 (2012). URL https://doi.org/10.1088%2F1748-9326%2F7%2F4%2F044035.

[40] Cubasch, U. *et al.* Time-dependent greenhouse warming computations with a coupled ocean-atmosphere model. *Climate Dynamics* **8**, 55–69 (1992). URL https://doi.org/10.1007/BF00209163.

[41] Hasselmann, K. F. *et al.* Detection of anthropogenic climate change using a fingerprint method (1995). URL https://pure.mpg.de/pubman/faces/ViewItemOverviewPage.jsp?itemId=item_2534307.

[42] Roeckner, E. *et al.* The atmospheric general circulation model ECHAM4: Model description and simulation of present-day climate. Report, Max-Planck-Institut für Meteorologie (1996). URL http://centaur.reading.ac.uk/31813/.

[43] Murphy, J. M. Transient Response of the Hadley Centre Coupled Ocean-Atmosphere Model to Increasing Carbon Dioxide. Part 1: Control Climate and Flux Adjustment. *Journal of Climate* **8**, 36–56 (1995). URL https://journals.ametsoc.org/doi/abs/10.1175/1520-0442%281995%29008%3C0036%3ATROTHC%3E2.0.CO%3B2.

[44] Murphy, J. M. & Mitchell, J. F. B. Transient Response of the Hadley Centre Coupled Ocean-Atmosphere Model to Increasing Carbon Dioxide. Part II: Spatial and Temporal Structure of Response. *Journal of Climate* **8**, 57–80 (1995). URL https://journals.ametsoc.org/doi/10.1175/1520-0442%281995%29008%3C0057%3ATROTHC%3E2.0.CO%3B2.

[45] Gordon, H. B. & O'Farrell, S. P. Transient Climate Change in the CSIRO Coupled Model with Dynamic Sea Ice. *Monthly Weather Review* **125**, 875–908 (1997). URL https://journals.ametsoc.org/doi/10.1175/1520-0493(1997)125%3C0875%3ATCCITC%3E2.0.CO%3B2.

[46] Washington, W. M. & Meehl, G. A. High-latitude climate change in a global coupled ocean-atmosphere-sea ice model with increased atmospheric CO2. *Journal of Geophysical Research: Atmospheres* **101**, 12795–12801 (1996). URL https://agupubs.onlinelibrary.wiley.com/doi/abs/10.1029/96JD00505.

[47] Manabe, S. & Stouffer, R. J. Multiple-Century Response of a Coupled Ocean-Atmosphere Model to an Increase of Atmospheric Carbon Dioxide. *Journal of Climate* **7**, 5–23 (1994). URL https://journals.ametsoc.org/doi/10.1175/1520-0442%281994%29007%3C0005%3AMCROAC%3E2.0.CO%3B2.

[48] Boer, G. J. *et al.* Some results from an intercomparison of the climates simulated by 14 atmospheric general circulation models. *Journal of Geophysical Research: Atmospheres* **97**, 12771–12786 (1992). URL https://agupubs.onlinelibrary.wiley.com/doi/abs/10.1029/92JD00722.

[49] Flato, G. M. *et al.* The Canadian Centre for Climate Modelling and Analysis global coupled model and its climate. *Climate Dynamics* **16**, 451–467 (2000). URL https://doi.org/10.1007/s003820050339.

[50] Tokioka, T. *et al.* A transient CO_2 experiment with the MRI CGCM - Annual mean response. Tech. Rep. CGER–1022-96, National Institute for Environmental Studies (1996). URL http://inis.iaea.org/Search/search.aspx?orig_q=RN:39063264.

[51] Emori, S. *et al.* Coupled Ocean-Atmosphere Model Experiments of Future Climate Change with an Explicit Representation of Sulfate Aerosol Scattering. *Journal of the Meteorological Society of Japan. Ser. II* **77**, 1299–1307 (1999). URL https://www.jstage.jst.go.jp/article/jmsj1965/77/6/77_6_1299/_article.

[52] Leggett, J. A., Pepper, W. J. & Swart, R. J. *Climate Change 1992. The Supplementary Report to the IPCC Scientific Assessment.* (Cambridge University Press, 1992).

[53] Taylor, K. E., Stouffer, R. J. & Meehl, G. A. An Overview of CMIP5 and the Experiment Design. *Bulletin of the American Meteorological Society* **93**, 485–498 (2011). URL https://journals.ametsoc.org/doi/abs/10.1175/BAMS-D-11-00094.1.

[54] Hansen, J., Ruedy, R., Sato, M. & Lo, K. Global surface temperature change. *Reviews of Geophysics* **48** (2010). URL https://agupubs.onlinelibrary.wiley.com/doi/full/10.1029/2010RG000345.

[55] Team, G. Giss surface temperature analysis (gistemp). https://data.giss.nasa.gov/gistemp/. Accessed: 2019-03-15.

[56] Cowtan, K. *et al.* Robust comparison of climate models with observations using blended land air and ocean sea surface temperatures. *Geophysical Research Letters* **42**, 6526–6534 (2015). URL https://agupubs.onlinelibrary.wiley.com/doi/10.1002/2015GL064888.

[57] Forster, P. M. *et al.* Evaluating adjusted forcing and model spread for historical and future scenarios in the CMIP5 generation of climate models. *Journal of Geophysical Research: Atmospheres* **118**, 1139–1150 (2013). URL https://agupubs.onlinelibrary.wiley.com/doi/10.1002/jgrd.50174.

Acknowledgements

We acknowledge the World Climate Research Programme's Working Group on Coupled Modelling, which is responsible for CMIP, and we thank the climate modeling groups for producing and making available their model output. For CMIP the U.S. Department of Energy's Program for Climate Model Diagnosis and Intercomparison provides coordinating support and led development of software infrastructure in partnership with the Global Organization for Earth System Science Portals. We thank Susan Solomon and Nick Lutsko for feedback on an earlier draft of the manuscript.

Author Contributions

All authors interpreted the data and wrote the paper. H.F.D. and T.A. conceived of the work; H.F.D. performed the data analysis.

Author Information

Reprints and permissions information is available at www.nature.com/reprints. The authors declare no competing interests. Correspondence and requests for materials should be addressed to henrifdrake@gmail.com.

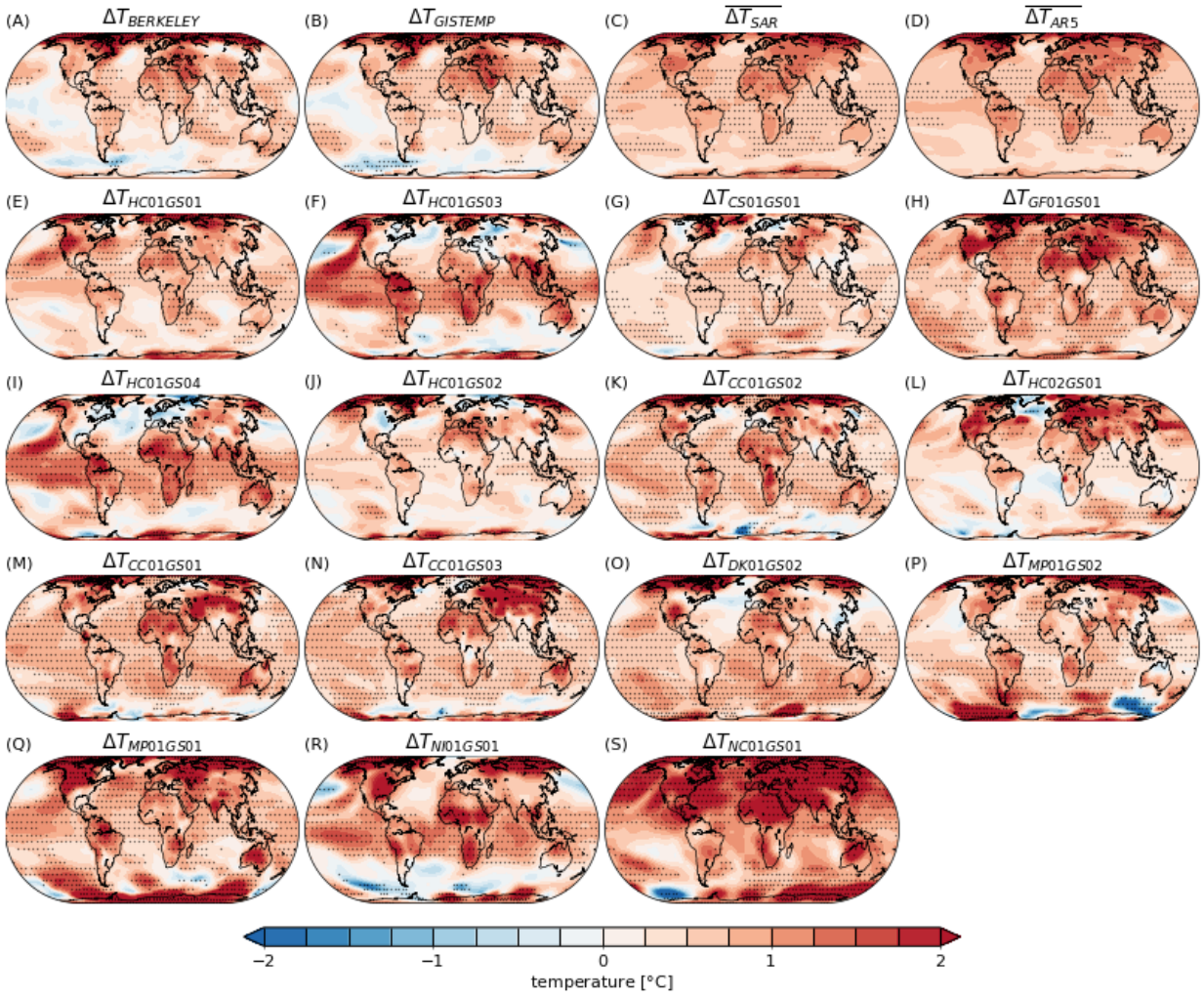

Extended Data Figure 1: Projected and observed spatial patterns of warming trends over the 1990-2018 nowcast period for (A) the Berkeley Earth observations, (B) the GISTEMP observations, (C) the SAR multi-model mean, (D), the AR5 multi-model mean, and (E-S) each individual SAR model. Stippling shows where the absolute temperature trend signal has emerged above the noise of inter-annual variability, $|\Delta T| > 2\sigma$, where σ is defined as the standard deviation of the annual-mean temperature timeseries with the nowcast linear trend removed, for each product. See Figure 2 for trends over the 1920-1990 hindcast period and Figure 3 for trends over the 1990-2100 forecast period.

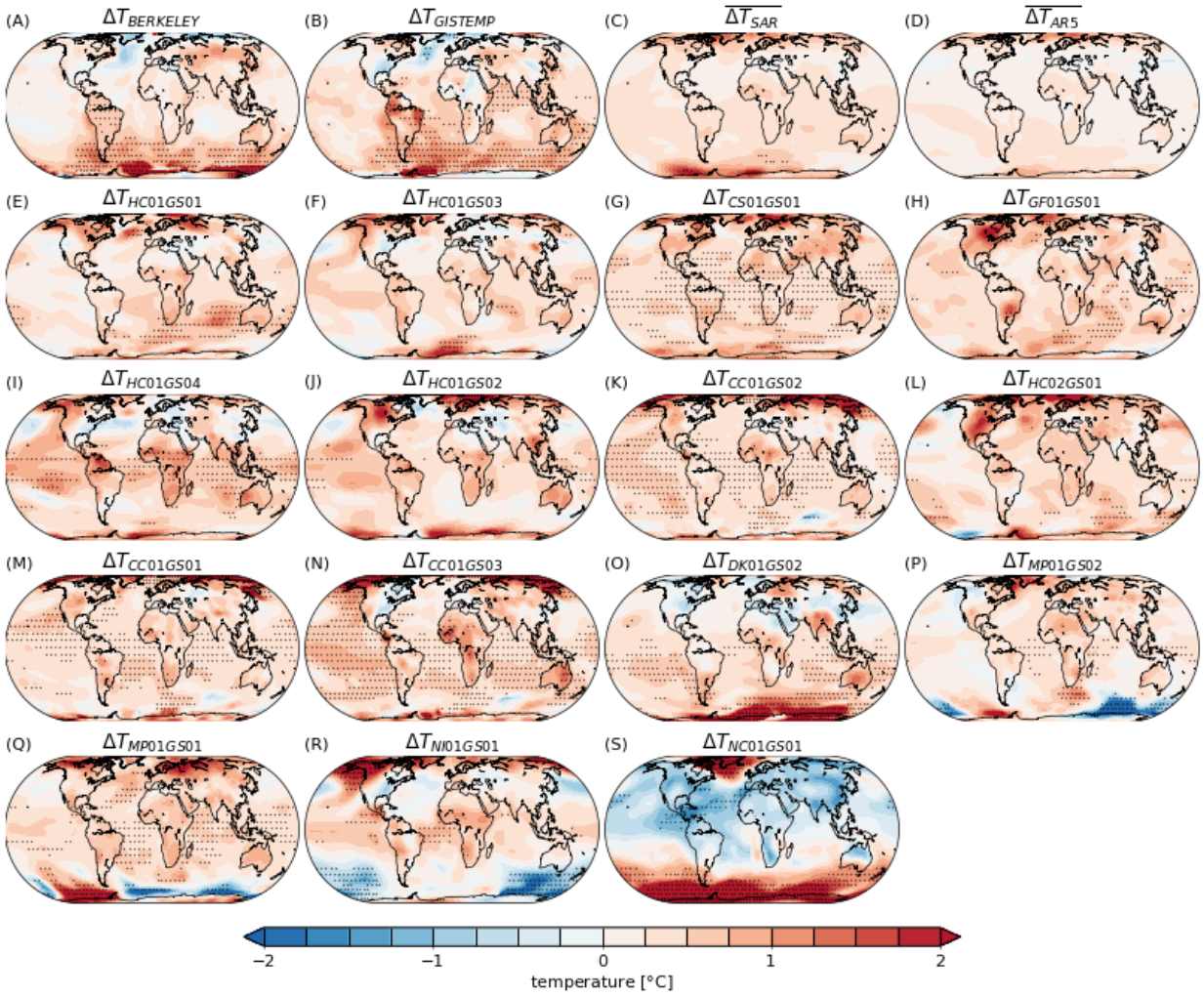

Extended Data Figure 2: Projected and observed spatial patterns of warming trends over the 1920-1990 hindcast period for (A) the Berkeley Earth observations, (B) the GISTEMP observations, (C) the SAR multi-model mean, (D), the AR5 multi-model mean, and (E-S) each individual SAR model. Stippling shows where the absolute temperature trend signal has emerged above the noise of inter-annual variability, $|\Delta T| > 2\sigma$, where σ is defined as the standard deviation of the annual-mean temperature timeseries with the hindcast linear trend removed, for each product.

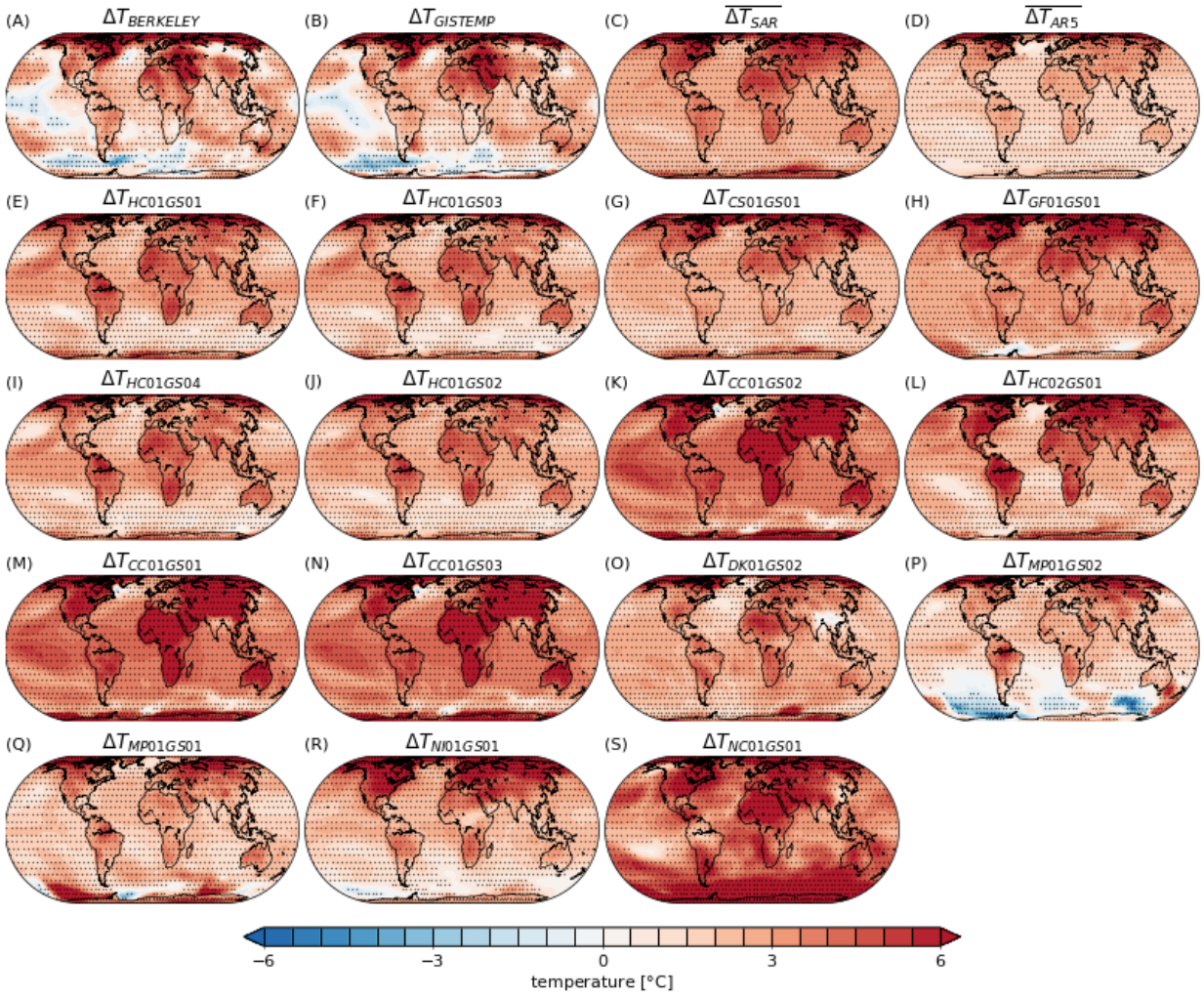

Extended Data Figure 3: Projected and observed spatial patterns of warming trends over the 1990-2100 forecast period for (A) the Berkeley Earth observations, (B) the GISTEMP observations, (C) the SAR multi-model mean, (D), the AR5 multi-model mean, and (E-S) each individual SAR model. For the observations (A) and (B), we linearly extrapolate the 1990-2018 nowcast trend for heuristic comparison with models. Stippling shows where the absolute temperature trend signal has emerged above the noise of inter-annual variability, $|\Delta T| > 2\sigma$, where σ is defined as the standard deviation of the annual-mean temperature timeseries with the forecast linear trend removed, for each product.

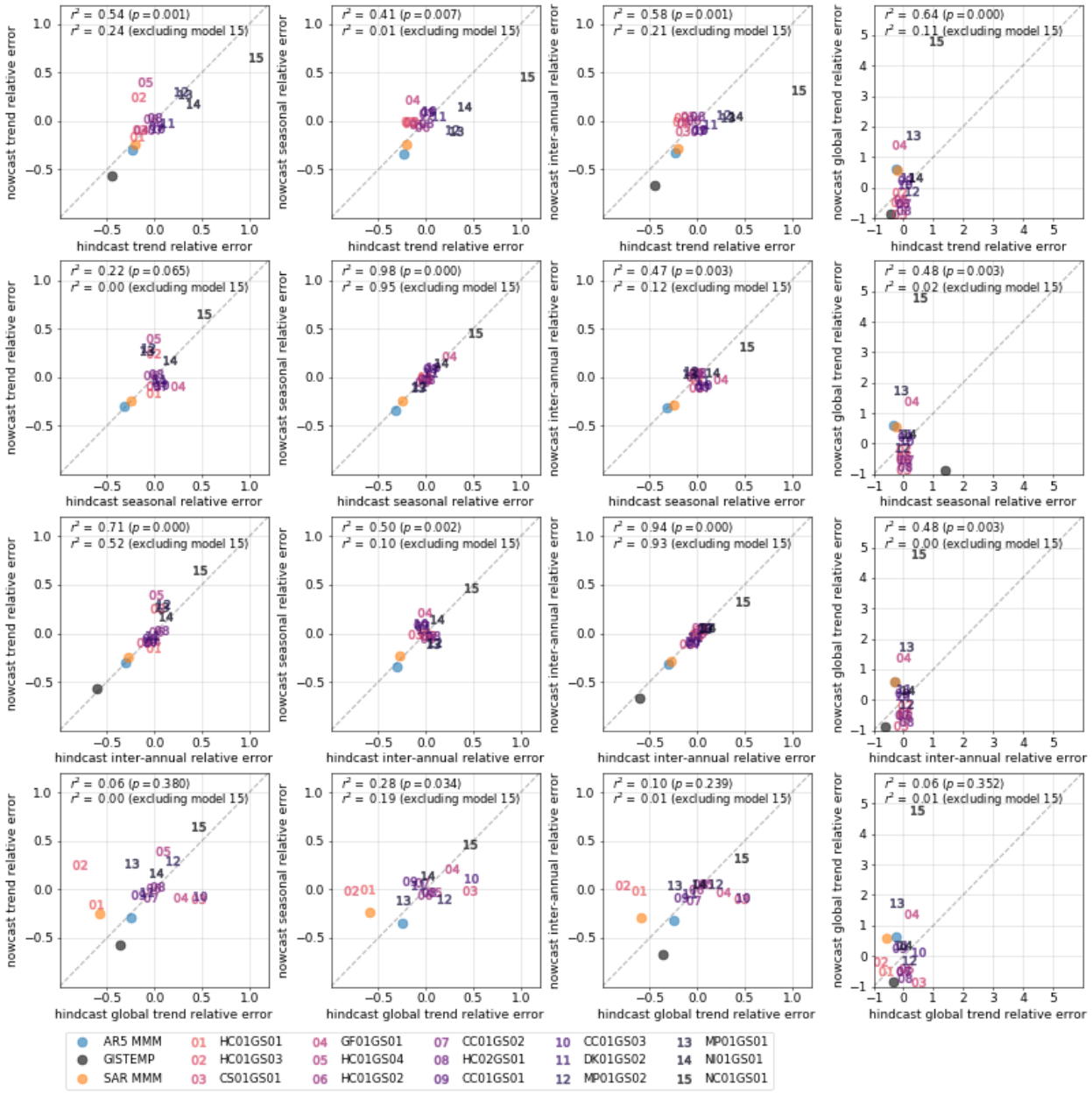

Extended Data Figure 4: Correlations between skill metrics for 1920-1990 hindcast and 1990-2018 nowcast. Y-axes show the skill metrics for the nowcast and x-axes show skill metrics for the hindcast. The four skill metrics shown are: (A) a spatially-resolved temperature trend metric, (B) a temperature seasonality metric, (C) an inter-annual temperature variability metric, and (D) a global-mean temperature trend metric. Large negative values indicate high model skill (see Methods for details). We show (blue) the AR5 multi-model mean, (black) the GISTEMP observations, (orange) the SAR multi-model mean, and (1-15) each individual model. Coefficients of determination r^2 are calculated (upper) by excluding GISTEMP and AR5 MMM and (lower) additionally excluding the outlier model NC01GS01. Note the change in axis scales for the right-most column.

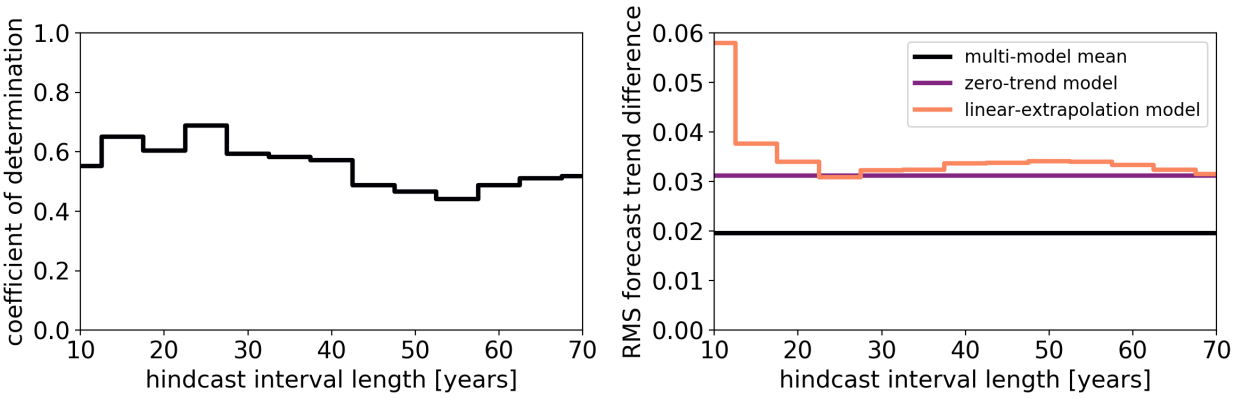

Extended Data Figure 5: (Left) Coefficients of determination for nowcast trend relative error against hindcast trend relative error (e.g. Figure 3A, upper) as a function of hindcast interval length (all ending in 1990). (Right) Root-mean square difference between model trend forecast and Berkeley Earth trend forecast for the multi-model mean and two heuristic reference cases: a uniformly-zero trend case and a linear extrapolation case. The hindcast interval length (always ending at 1990) is varied from 10 years to 70 years to show that the relative skill of the multi-model mean to the extrapolation case is independent of the period over which the hindcast trend is calculated.

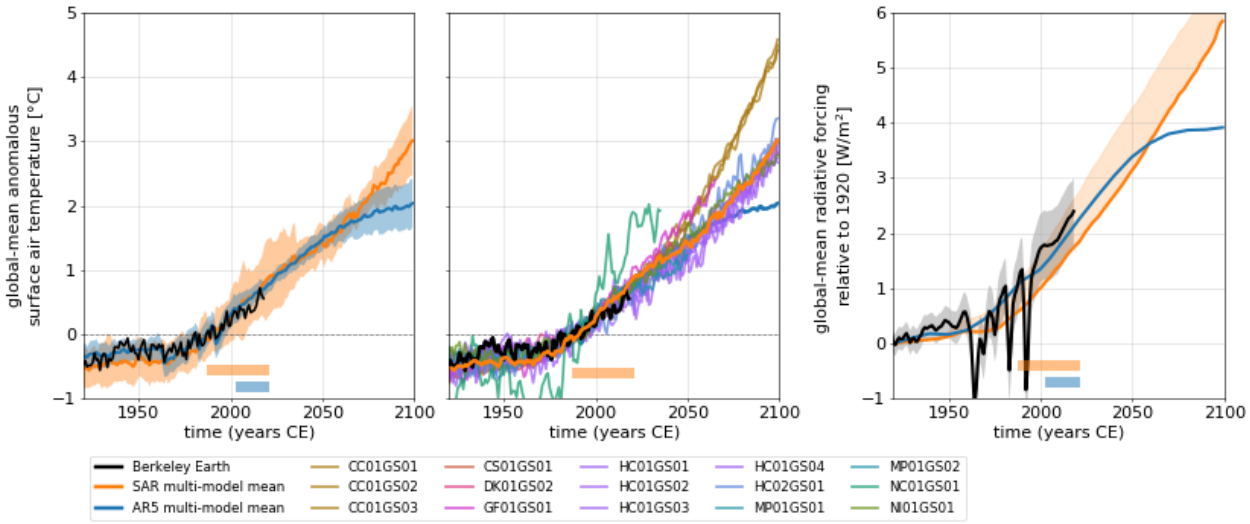

Extended Data Figure 6: Projected and observed global annual mean surface air temperature anomalies and radiative forcing. (Left) Global annual mean surface air temperature anomalies relative to the 1985-1995 mean. Solid lines show the (black) Berkeley Earth observations, (orange) SAR multi-model mean, (blue) AR5 multi-model mean. Orange and blue shading show the SAR and AR5 multi-model means $\pm\varsigma$, respectively, where ς is the inter-model standard deviation. (Middle) Global annual mean surface air temperature anomalies relative to the 1985-1995 mean for each individual SAR model where colors indicate different models. (Right) Global mean radiative forcing relative to 1920. Solid lines show our estimates of historical, SAR model, and AR5 (following the RCP4.5 scenario) forcing and the shading shows uncertainty estimates (see Methods for details). The orange bars delineate the 1990-2018 SAR nowcast period and the blue bars delineate the 2005-2018 AR5 nowcast period. Note that the abrupt decrease in SAR model spread around 2033 in the left panel is due to the end of the outlier projection from the NC01GS01 model.

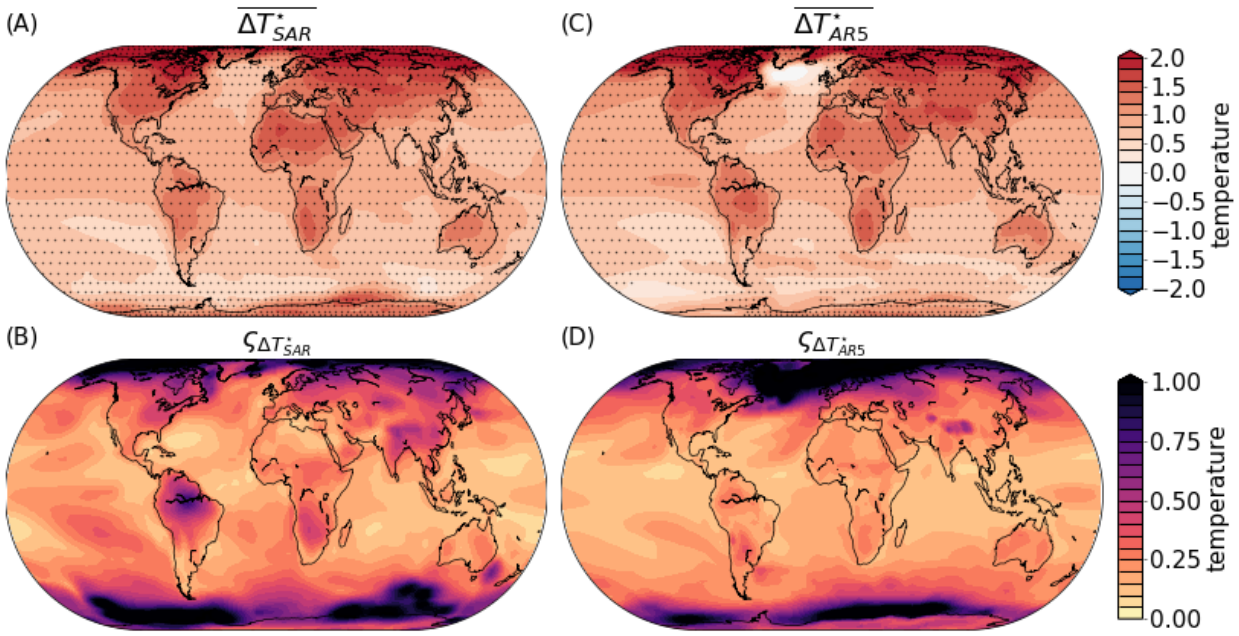

Extended Data Figure 7: (Left) Multi-model mean spatial patterns of normalized temperature trends over the 1990-2100 forecast period for the (A) SAR and the (C) AR5. Stippling shows where the multi-model mean absolute temperature change $|\Delta T|$ is more than twice the multi-model mean inter-annual variability σ (as in Figure 2). (Right) Inter-model standard deviation ς of the normalized temperature trends for the (B) SAR and the (D) AR5. Each individual model's temperature trends are normalized by its global mean temperature trend.